Article:

Corredor-Garcia, J.L., Stovin, V. and Guymer, I. orcid.org/0000-0002-1425-5093 (2025) Hydrodynamics and length-scale distributions of a random cylinder array. ASCE Journal of Hydraulic Engineering, 151 (1). ISSN 0733-9429

https://doi.org/10.1061/JHEND8.HYENG-13872

Hydrodynamics and Length-Scale Distributions of a Random Cylinder Array

Jesus Leonardo Corredor-Garcia, Ph.D.[1], Virginia Stovin, Ph.D.[2], and Ian Guymer, Ph.D.[3]

[1]Postdoctoral Research Associate. Dept. of Civil and Structural Engineering, Univ. of Sheffield, Mappin St., Sheffield S1 3JD. Email: j.l.corredor.garcia@sheffield.ac.uk

[2]Professor of Green Infrastructure for Stormwater Management. Dept. of Civil and Structural Engineering, Univ. of Sheffield, Mappin St., Sheffield S1 3JD. Email: v.stovin@sheffield.ac.uk

[3]Professor of Civil Engineering. Dept. of Civil and Structural Engineering, Univ. of Sheffield, Mappin St., Sheffield S1 3JD. Email: i.guymer@sheffield.ac.uk

ABSTRACT

In vegetated flows a reliable estimation of flow scales is crucial to understand and model mixing processes. This study presents velocity maps obtained using Particle Image Velocimetry (PIV) within a cylinder array (diameters $4 \leq d \leq 20$ mm) designed to mimic real emergent vegetation. Tests were undertaken over a comprehensive range of stem Reynolds numbers ($100 \leq Re_d \leq 900$), intended to characterise time-dependent hydrodynamic features, including their interactions. Time-averaged flow heterogeneities are found to be independent of Re_d. Vortex dynamics are seen to dominate turbulent fluxes of momentum, and are the relevant coherent structures driving mass transport. The range of characteristic time- and length-scales from these coherent structures was quantified and shown to be determined by the distribution of spaces between cylinders. This is due to: (i) neighbouring cylinders forming clusters, leading to larger flow structures, and (ii) the maximum size of the flow structures being constrained by the inter-stem space. It is concluded that the Delaunay criterion provides practitioners with a good approximation to the distribution of flow scales in vegetated flows.

Practical Applications

This study presents the quantification of the scales of flow structures generated in a vegetated flow. These structures play an important role in the quantification of mass transport processes, and estimates of the sizes of these flow structures are necessary to understand the rate of solute transport and therefore provide reliable model for pollutant mixing in vegetated flows. Using state-of-the-art equipment to characterise velocity fields, the present study found that the size of these flow structures is determined by the spacing between cylinders. The author's recommend that for practical applications, engineers quantify the spacing between plant stems using the criteria presented in this paper.

INTRODUCTION

Literature Review

Aquatic vegetation in natural streams dominates a wide range of physical, biochemical and restoration processes. It influences sediment dynamics (Righetti and Armanini 2002), which impacts stream geomorphology (Simon et al. 2004). Vegetation elements affect flow resistance (Jalonen and Järvelä 2014), govern the rates of mass and momentum exchange (Nepf 2012), and influence the rates of nutrient uptake and biochemical reactions (Nishihara and Terada 2010). The consequences of these processes are fundamental for stream restoration, conservation, biota reproduction, water quality control, and stormwater management (Shilton 2000).

In open channel flow, bed effects govern the transfer of mass and momentum. For emergent vegetation, experimental results have shown that bed effects are confined to a smaller bed region (Nepf et al. 1997b) and the vertical transfer of momentum, and vertical gradients of streamwise velocities (dU/dz), are negligible over the flow depth (Ricardo et al. 2016b). Therefore, emergent vegetation flows can be considered a special case of shallow 2D flows (Jirka and Uijttewaal 2004).

From experiments using cylinder arrays to simulate the stems of emergent vegetation, the time-averaged flow fields are characterised by cylinder-induced features: wakes, boundary layers and advective acceleration regions (White and Nepf 2003; Nepf 2012). These features create a heterogeneous flow field with zones of high and low velocities (differential advection) that contribute to the proportional spread of mass along vegetated reaches (Sonnenwald et al. 2017). Cylinder wakes are divided into near- and far- regions (called secondary wakes in White and Nepf 2003). The length of near-wakes (cf. formation regions) is a function of diameter, d, and local Reynolds number, Re_d, and independent of array density, φ. Measurements of the formation region length, obtained from single-cylinder flow experiments, have yielded estimates between $1d$ to $2d$ (Gerrard 1978).

Cylinder-induced turbulence overshadows that generated from the bed, and the difference increases proportionally with stem density, φ (Nepf 1999; Nepf et al. 1997a). Ricardo et al. (2014a) quantified the terms of the Turbulent Kinetic Energy (TKE) equation from local measurements using Particle Image Velocimetry (PIV) and Laser Doppler Anemometry (LDA). Vortex dynamics were found to be the main drivers of Turbulent Kinetic Energy (TKE) production, in the inter-stem space. A local peak in TKE production occurs the limit of the near-wake, and turbulent diffusion and fluxes are subsequently directed downstream into the far-wake. No local production-dissipation equilibrium was found in the inter-stem space (Ricardo et al. 2014a). Further, turbulent stresses were found to adapt to local density and are therefore independent of longitudinal stem density gradients ($d\varphi/dx$) (Ricardo et al. 2016b).

Experimental limitations have precluded comprehensive analyses on the range of flow scales existing in cylinder arrays. Quantifying the sizes of the dominant coherent structures in these environments is a key component in the hydrodynamic characterisation of obstructed flows. These structures represent the integral scales and thus govern the rates of turbulent mass and momentum transfer, and are key in the determination of mixing lengths. In cylinder arrays these relevant scales are connected to the rates of lateral spread due to mechanical dispersion (Nepf 1999; Tanino and Nepf 2008b; and Tanino and Nepf 2009); and the extent of the advective zone, which is the distance necessary for a scalar to lose correlation with its initial position and disperse in a Fickian manner (Shucksmith et al. 2007). Further, a characteristic scale that represents the effects of cylinder arrays on the flow, at the reach scale, is necessary to apply dimensional analysis on obstructed flows and formulate closure models for numerical experiments (Ricardo 2014; Juang et al. 2008).

For engineering practice, it is desirable to obtain estimates of these flow scales, directly from the morphology of the cylinder array. Conventionally, the main flow scales in cylinder arrays are estimated as the smaller between the mean diameter, d, and the average space between each cylinder and its nearest neighbour, s_n (Nepf 2012). Flow features are assumed to scale with the mean diameter, d, since turbulence is generated in the wakes of each cylinder (Nepf 1999). In dense arrays, however, these flow structures will be dissipated in the spaces between cylinders, at scales smaller than the diameter (Tanino and Nepf 2008a).

Ricardo (2014) presented estimates of length scales within the inter-stem space in cylinder arrays, using spatial autocorrelations of mean velocity. This approach suggested flow scales to be proportional to the mean transverse distance between adjacent cylinders. Also, Ricardo (2014) concluded that the integrational approach to estimate length scales from temporal features (Taylor 1922) does not apply for coherent flows, as the periodicity can generate unrealistic estimates and even negative values (Csanady 1973). The dominant period in these coherent functions is seen to be a more appropriate estimate of time scales.

The use of the minimum of either d or s_n (Nepf 2012) presupposes that the flow field is the result of linear superpositions of the effects of individual cylinders. This overlooks the existence of flow structures larger than those generated from single elements (Sumner 2010). Further, the method presented in Ricardo (2014) tends to mask the temporal variation (i.e. characteristic periods) of travelling structures, as it removes the coherence component of the velocity series analysed. In summary, previous physical assumptions for the definitions of d and s_n as relevant scales need to be reviewed experimentally. A unified methodology for the determination of a spacing distribution, that considers a wider range of flow scales, from cylinder interactions, is needed. These challenges will be explored in this study, using time-dependent velocity statistics from the comprehensive velocity maps obtained, and appropriate formulations for the estimation of relevant flow scales, based on array morphology will be given.

The Double-Average Framework

Equations for the momentum, mass and energy balance serve as a starting point to study the way in which instantaneous flow variables are related. Averaging frameworks simplify the analysis of flow equations by removing degrees of freedom that, due to experimental limitations, cannot be quantified directly (Nikora et al. 2007). The analysis presented here is based on the momentum equation, which expresses a balance between flow acceleration and the forces acting on the flow field. Using index notation, the general momentum equation is defined as

$$\frac{\partial}{\partial t}u_i + u_j\frac{\partial}{\partial x_j}u_i = \frac{\partial}{\partial x_j}\left(-\frac{1}{\rho}p\delta_{ij} + \nu\frac{\partial}{\partial x_j}u_i\right) + f_i \quad (1)$$

where p is the instantaneous pressure, i and j are the indices indicating each spatial direction,

δ_{ij} is the Kronecker delta, ν the kinematic viscosity for the fluid and ρ its density, and f_i the external force term (Hinze 1975). Similar to the framework for the RANS equation (Pope 2000), a double-average framework can be applied to generate virtual stress terms that represent the effects of the vegetation-induced temporal and spatial fluctuations (Nikora et al. 2013).

$$\epsilon \left\langle \overline{u_j} \right\rangle \frac{\partial}{\partial x_j} \left\langle \overline{u_i} \right\rangle = \frac{\partial}{\partial x_j} \epsilon \left(-\frac{1}{\rho} \left\langle \overline{p} \right\rangle \delta_{ji} + \left\langle \nu \frac{\partial \overline{u_i}}{\partial x_j} \right\rangle - \left\langle \overline{u_i}'' \overline{u_j}'' \right\rangle - \left\langle \overline{u_i' u_j'} \right\rangle \right) + \epsilon \left\langle \overline{f_i} \right\rangle + \left(\frac{1}{\rho} \right) \frac{1}{V_f} \overline{\int_{S_C} n_i \, p \, dS} - \frac{1}{V_f} \overline{\int_{S_C} n_j \, \nu \frac{\partial u_i}{\partial x_j} \, dS} \tag{2}$$

The overbar, $\overline{\cdot}$, represents a time average, and the operator $\langle \cdot \rangle$ represents a spatial average over an area large enough to be representative of the reach scale. Each instantaneous variable u_i is replaced by its double-averaged decomposition, $u_i = \langle \overline{u_i} \rangle + \overline{u_i}'' + u_i'$ (Nikora et al. 2013). The terms n_i represent each component of the unit vector normal to each cylinder surface, V_f is the averaging volume, and S_C is the surface of each cylinder. Eq. (2) includes the effects of pressure (form) and viscous drag (6th and 7th terms on the RHS) on the momentum balance as independent terms. The velocity heterogeneities are summarised in the covariance term $\left\langle \overline{u_i}'' \overline{u_j}'' \right\rangle$, and referred to as form-induced stresses (Giménez-Curto and Corniero Lera 1996) or dispersive fluxes (Raupach et al. 1986). The effects of turbulence are expressed in the covariance term $\left\langle \overline{u_i' u_j'} \right\rangle$, called turbulent stresses (Nikora et al. 2013), and ϵ represents the porosity ($\epsilon = 1 - \varphi$).

The interpretation of the terms $\left\langle \overline{u_i}'' \overline{u_j}'' \right\rangle$ and $\left\langle \overline{u_i' u_j'} \right\rangle$ as stresses comes from the idea that their effect on a fluid volume is similar to that of viscous stresses as a representation of molecular momentum transfer (Pope 2000). Similarly, these terms express the average flux of directional momentum due to turbulence and flow heterogeneities, between flow layers, over the area of analysis, and can therefore be also interpreted as turbulent and dispersive momentum fluxes. These momentum fluxes can help describe characteristic dispersive length scales due to turbulence and differential advection. For consistency and simplicity, these terms will be referred to as turbulent and dispersive fluxes throughout the paper.

Objectives

To date, experimental limitations have precluded the possibility of obtaining detailed characterisations of vegetated velocity fields. As a step forward in the characterisation of hydrodynamics in vegetated flows, this study presents the results of velocity field measurements, using a Particle Image Velocimetry (PIV) system that allowed for the illumination of a Field of View (FoV) large enough to cover the reach-average morphological parameters of a random cylinder array, with a resolution that also permitted the study of velocities over small areas around individual cylinders. This new cylinder array, named RandoSticks, incorporates a diameter distribution, designed to mimic the distribution of stem sizes (diameters) and spacing observed in characterisations of winter *Typha Latifolia* (Sonnenwald et al. 2017).

The aim of this study is to provide a full description of vegetated hydrodynamics in an artificial array, to estimate turbulence structures, and describe mass and momentum fluxes. This research focuses on the variation of these quantities with Reynolds number, Re_d, for a single physical configuration. The results offer a complete picture of inter-stem hydrodynamics, and of the influence of cylinder interactions on the size and behaviour of flow structures. These new insights will provide practitioners with relevant, physically-based information to determine appropriate distributions of length scales to model mass transport in vegetated flows. The following specific objectives will be explored:

- Identify the main spatial features of the vegetated flow field, via qualitative analysis of 1st (temporal mean) and 2nd order (deviations from the mean) velocity maps, e.g. wakes, zones of turbulence production. Characterise the changes in these quantities with Reynolds number, and identify the physical processes generating these features.

- Quantify the fluxes of mass and momentum in a double-averaged (DA) sense, and relate them to the general morphological parameters of the cylinder array and the different flow regimes considered during the experiments.

- Quantify the main flow scales driving the transport of mass, and relate them to the morphological descriptors of the RandoSticks array.

The Methodology Section outlines the experimental system, and the techniques used, which are presented in more detail in Corredor-Garcia et al. (2022) and Corredor-Garcia (2023). The Results Section shows horizontal 2D maps of time-averaged velocity fields, from which the relevant double-averaged quantities are obtained. Finally, time-dependent velocity statistics are analysed to obtain the characteristic shedding frequencies and length scales at representative points within the flow field. New insights into the range of flow structures and their generation mechanisms are provided.

METHODOLOGY

Experimental Facilities

The experiments were performed in a 14 m-long by 1 m-wide flume in the Water Engineering Laboratory at the University of Sheffield, which had a fixed slope of $\beta = 0.138‰$. The flow for the experiments was provided by a constant-head tank, and controlled using an inlet valve. The temperature during the experiments was on average 17.8 °C (kinematic viscosity, $\nu = 1.06 \cdot 10^{-6}$ m^2/s). All tests were conducted with a reference water depth of 150 mm in the PIV Field of View (shown as a $\times$ in Figure 1b). Photos and a detailed description of the equipment, calibration and preparation methods are presented in Corredor-Garcia et al. (2022) and Corredor-Garcia (2023).

RandoSticks Configuration

The RandoSticks diameter distribution (d = 4, 8, 12, 15, 20 mm), was designed to replicate real measurements from winter *Typha Latifolia* (Sonnenwald et al. 2017), and is presented in Figure 1a. The cylinders comprising the distribution were organised in a 1.0×1.0 m^2 pattern of randomly located PVC cylinders (Figure 1b), replicated over 9 m along the flume. The average physical parameters of the RandoSticks array in the area of study (PIV Field of View, Figure 1c) are: mean diameter, $d = 10.35$ mm; solid volume fraction, $\varphi = 0.05$; stem number density, $n = 506$ stems/m^2; frontal facing area per unit volume of vegetation $a = 5.08$ m^{-1}.

The RandoSticks array started 2.92 m downstream from the flume inlet, and covered a total of 9 m downstream. Seeding particles for PIV were injected 2 m downstream from the start of the RandoSticks array (i.e. 4.92 m from the flume inlet), to allow the flow to stabilise before the injection and measurement areas. The injection location is chosen as the origin of the global coordinate system (X_{rs}, Y_{rs}) in the streamwise location, i.e. $X_{rs} = 0$. The PIV Field of View (FoV), with dimensions $\Delta X = 0.32$ m and $\Delta Y = 0.52$ m, was centred at $X_{rs} = 1.50$ m downstream from the seeding injection location, and at a lateral distance $Y_{rs} = 0.57$ m from the right wall of the flume. To allow visualisation from underneath the flume, the FoV was fitted with a glass window below a 0.33×1.00 m^2 acrylic plate. This acrylic plate was perforated to place glass cylinders and tubes such that the laser plane needed for the PIV measurements, located at mid-depth (75 mm), was able to illuminate between cylinders. The location of this acrylic plate, relative to the injection point, and the PIV Field of View are shown in Figures 1b and c. Figure 1c also shows the locations and labels of the points used to illustrate the differences in autocorrelation periods, and thus length scales, presented in the Shedding Frequency and Length Scales sections below. These points represent the locations of the end of the recirculation region, along cylinder wakes, estimated from previous studies (Gerrard 1978).The ellipses around each selected cylinder represent the length of the recirculation zone, and the points where the velocity series were analysed are denoted with a '×' symbol. The dotted rectangle in Figure 1c is the reference area chosen to illustrate the definitions of inter-stem spacing given in Figure 7.

PIV Set-up

Glass tubes ($d = 12, 15, 20$ mm) and rods ($d = 4, 8$ mm) were used to allow visualisation within the Field of View shown in Figure 1c. These were made of borosilicate glass 3.3 (refractive index of 1.473; Schott 2017). In total, 6 tests were performed with the following mean velocities: $U =$ 12.8, 26.2, 34.3, 42.2, 68.3, and 88.6 mm/s; and the corresponding diameter Reynolds numbers: $Re_d = 125$, 256, 335, 412, 667, and 865.

The value of the Reynolds number, Re_d reported is based on the mean cylinder diameter, $d = 10.35$ mm, within the Field of View (Figure 1c). The camera used in the PIV set-up is a

Blackfly BFS-U3-23S3 machine vision (FLIR 2018), fitted with a short focal-length (i.e. 48 mm) lens (Computar 2018), to capture the relatively large FoV. The illumination system consisted of a CNI, 10 W laser, operating at 532 nm, fitted into a scanning laser sheet generator (scanning periods in the range: 225 - 750 μs), that created a horizontal plane 75 mm from the channel bed, to measure x and y components of the mid-depth velocity field. To avoid secondary scanning effects in the images, the camera shutter times, frame rate and laser scanning box rate were synchronised (i.e. multiples of each other). The seeding used was polyamide 12 (density, 1.05 g/cm^3) with combined diameters of 20 and 100 μm.

For each test, 16000 images, with a resolution of 1996 × 1258 pixels, were taken. Note that due to the short focal-length lens used, image distortion occurred, and areas around cylinders were blocked due to perspective errors. A piecewise linear transformation was used to correct lens distortion (Higham and Brevis 2019). The camera allowed for an acquisition frequency of 65 fps. Four passes with interrogation windows of 120, 60, 32 and 16 pixels, with an overlap of 50% between consecutive frames, were used for the calculation of velocities. Pre-processing, calculation and post-processing of the displacement information was done using PIVlab (Thielicke and Stamhuis 2014; Thielicke and Sonntag 2021). An additional pre-processing algorithm to account for the glass-generated illumination heterogeneities was applied to equalise the intensity response in all areas of the PIV images (Corredor-Garcia et al. 2022).

RESULTS

Velocity Characterisation in the RandoSticks Configuration

Mean velocities (1st order quantities)

Figure 2a and 2b show the time-averaged streamwise and lateral velocity maps ($U(x, y) = \overline{u}$ and $V(x, y) = \overline{v}$), normalised by reach-averaged velocity ($U^*(x, y) = U(x, y)/\langle\overline{u}\rangle$). Wakes can be identified in Figure 2a as the zone of low velocities ($U^*(x, y) < 1$) behind individual cylinders, and are more noticeable for cylinders that tend to group together, as shown in the area circled as A. Preferential paths of high velocity ($U^*(x, y) > 1$) are generated between groups of stems, as can be seen in circle B of Figure 2a. The normalised, time-averaged lateral velocity map, V^* (Figure 2b) shows larger magnitudes of lateral displacement within groups of stems than around isolated ones.

The time-averaged features were found to be consistent for all Re_d tested. This is corroborated by the probability distributions of the mean velocity maps $U^*(x, y)$ and $V^*(x, y)$ presented in Figure 2c and d, respectively. The probability distributions show that the spread of low and high velocity areas in the time-averaged velocity maps remain constant with Re_d. For all Re_d tested Figures 2c and d show that the average maps have the same proportion of wakes, recirculation zones and acceleration gaps for $U^*(x, y)$, and the same pattern of lateral displacements for $V^*(x, y)$. In other words, first-order hydrodynamic features are independent of Re_d in the RandoSticks configuration.

Turbulent Kinetic Energy (2nd order quantities)

Employing the Reynolds decomposition on the velocity maps, ($u_i = U_i + u'_i$), an estimation of the 2D TKE is obtained by time-averaging the squares of the turbulent fluctuations of velocity: $k = (\overline{u'^2} + \overline{v'^2})/2$. The magnitudes of this quantity show the combined effects of 'random' turbulence and coherent motions generated by vortex shedding, particularly their energy. Figure 3a shows that non-dimensional TKE values, $k^* = k/\langle\overline{u}\rangle^2$, reach local peaks downstream from the stems, at lengths that match the $\sim 1d$ distance reported by Ricardo et al. (2014a) and Ricardo et al. (2014b). This distance also matches the end of the recirculation region reported by Gerrard (1978). These peaks are expected near the sources of turbulent energy, which is transferred from the mean flow through cylinder drag.

The magnitude and spatial extent of the peaks of k^* are proportional to cylinder size, Re_d, and the presence of cylinders downstream. Figure 3a shows larger TKE peaks for isolated cylinders, compared with those closely followed by other cylinders, suggesting that the growth of coherent structures is constrained by the space between cylinders and increasing decay at larger Re_d.

Shear Reynolds stresses, $\tau_{xy} = \overline{u'v'}$, indicate momentum and mass transfer between flow layers (Pope 2000, Hinze 1975), particularly around obstructions. Understanding this transfer within the entire flow field helps interpret wake interactions in obstructed flows. Nondimensionalising shear Reynolds stresses by total turbulent momentum, $\tau^*_{xy} = \tau_{xy}/(u^+v^+)$, represented here by the root-mean-square of the streamwise and lateral turbulent fluctuations ($u_i^+ = \sqrt{\overline{u_i'^2}}$), provides a clearer visualisation of tangential momentum transfer at each point. Figure 3b shows the spatial distribution of this non-dimensional version of shear Reynolds stresses, τ_{xy}^*. Interacting wakes with opposite signs show no transfer, while those with the same signs coalesce. This is evident within the rectangle in Figure 3b, where the negative portion of an 8 mm wake coalesces with similar areas from 4-mm cylinders downstream. Similarly, the positive wake areas from three consecutive 4-mm cylinders merge together. However, when the negative transfer area from the 8 mm-cylinder wake encounters the positive area the three consecutive 4-mm cylinders, no shear momentum transfer between the wakes occur. This behaviour resembles collision-coalescence as reported by Ricardo et al. (2016a) and Ricardo et al. (2016c) for vorticity fluxes. Non-dimensional shear Reynolds stresses serve as a good indicator of wake extent, magnitude, and deformation. It is hypothesised that the cancellation of momentum transfer between adjacent wakes, when τ_{xy} has opposing signs, is an indication of no net momentum transfer between interacting wakes.

Contrary to the time-averaged maps shown in Figure 2a and b (i.e. $U^*(x, y)$ and $V^*(x, y)$, respectively), the maps of second order velocity statistics change with Re_d, as is evidenced in the probability distributions of k^* and τ_{xy}^* presented in Figure 3c and d. In particular, the distribution for $Re_d = 125$ shows k^* to be a more prominent than for the other tests. As will be explained in the section on Turbulent and Dispersive Fluxes, these variations are related to the changes in vortex dynamics that are dependent on Re_d. However, the results should only be considered from a qualitative perspective, as small displacements at $Re_d = 125$ tended to mix velocity fluctuations with noise inherent with PIV experiments. Note that in Figure 3a, not all cylinders of the same diameter show the same magnitudes for the peaks of Turbulent Kinetic Energy (TKE) production. This is caused by the effect of neighbouring cylinders on local turbulence production.

Turbulent and Dispersive Fluxes in the RandoSticks configuration

In the double-averaged momentum equation (Eq. 2), and the 2D flow assumption, horizontal instantaneous variables (u and v) are replaced by net momentum fluxes acting over the averaging area, i.e. the PIV Field of View. These fluxes are the velocity correlation terms $\left\langle \overline{u_i' u_j'} \right\rangle$ and $\left\langle \overline{u_i}'' \overline{u_j}'' \right\rangle$, which represent the net turbulent and dispersive momentum fluxes acting on the obstructed reach. The first term comprises random and coherent turbulent motions, and the second term represents the effects of (time-averaged) flow heterogeneities caused by the presence of cylinders. Figure 4 shows the variation of these fluxes with Re_d for all the tests conducted.

Normal Reynolds stresses, $\overline{u_i'u_i'}$, are an estimation of the square of the turbulent length scale for each point in the flow field. Their spatial average, $\left\langle\overline{u_i'u_i'}\right\rangle$, gives a representative turbulent scale for the cylinder array analysed, i.e. they represent the magnitude of the average coherent scales for the entire array. It can be seen from Figure 4 that normal turbulent momentum fluxes can be considered isotropic (i.e. equal magnitude in the x and y direction), while momentum fluxes ($\left\langle\overline{u'v'}\right\rangle$ and $\left\langle\overline{u}''\overline{v}''\right\rangle$) are clearly negligible in a double-averaged sense.

Non-dimensionalising turbulent and dispersive fluxes using the square of the mean velocity, $\langle\overline{u}\rangle^2$ (Figure 4b) shows that turbulent momentum fluxes decrease with Re_d, in the range ($125 < Re_d < 300$). Above this range, non-dimensional turbulent momentum fluxes remain relatively constant for the rest of the tests conducted ($300 < Re_d < 900$). Within this dataset, a local peak at $Re_d = 667$ can be seen. As will be pointed out below, this local peak is connected to transverse seiching for that test (i.e. periodic motions caused by a synchronisation between water surface fluctuations and cylinder shedding frequencies, Defina and Pradella 2014), and cannot be concluded to be universal.

A physical interpretation of the results for normal turbulent momentum fluxes, $\left\langle\overline{u_i'u_i'}\right\rangle$, in the range $125 < Re_d < 300$, may be made based on the results from single cylinders. The maximum value of turbulent momentum fluxes measured ($Re_d = 125$) is close to theoretical maximum value as it coincides with the onset of periodic vortex shedding (Gerrard 1978). Close to this value, it is known that the flow is dominated by a periodic vortex shedding regime, where turbulence production comes from a combination of vortex decay and a transition to turbulence in the wakes as they travel downstream (Roshko 1954; Gerrard 1978). The decreasing trend after this maximum can be attributed to a transition to three-dimensional, small-scale vorticity for $Re_d \approx 190$ (Williamson 1991), which is coupled with an accelerated break down of vortices due to the presence of downstream cylinders, and an increasing shedding frequency caused by shear (Kiya et al. 1980).

Non-dimensional dispersive fluxes show a moderate inverse proportionality with Re_d, which, in the case of $\langle \overline{u}''\overline{u}'' \rangle$, indicates a reduction of the size of the boundary layers and recirculation zones behind stems. Dispersive fluxes are anisotropic, as they do not represent the same scales. Streamwise dispersive fluxes, $\langle \overline{u}''\overline{u}'' \rangle$, represent the differences between boundary layers, trapping zones and wakes behind and around stems; and advective acceleration zones between cylinders. Transverse dispersive fluxes, $\langle \overline{v}''\overline{v}'' \rangle$, are proportional to the size of the cylinders, and as such are predominantly dependent on array morphology (Tanino and Nepf 2008b).

Shedding frequency in the RandoSticks configuration

As described in the Section on Turbulent and Dispersive Fluxes, the variation of reach-scale hydrodynamic quantities in the RandoSticks configuration is governed by vortex dynamics. Vortices are the dominant structures in cylinder flows, since both their frequency and characteristic length scale are expected to dominate the transfer of mass and momentum along cylinder arrays (Nepf 1999; White and Nepf 2003).

A sample of points was analysed to obtain representative values of the shedding frequency, f_s. The points were located at the end of the recirculation region ($\sim 2d$ downstream from the cylinder centre along the wake centreline, Gerrard 1978), for 32 different cylinders, chosen randomly. Figure 1c shows the RandoSticks FoV, with the location of a subsample, consisting of two cylinders, A and B per diameter, of the original 32-cylinder sample. The dominant flow structures within cylinder arrays are the vortices shed by the cylinders. To better visualise the coherence of the vortices contained within the array, a velocity autocorrelation function was calculated for all points. Note that these points are referred to specific cylinders, but as will seen below, these vortices are not solely determined by their reference cylinders in an array. The transverse velocity series was used, as this is shown to better reveal the vortex periods along the wake centrelines (Roshko 1954). For reference, the velocity autocorrelation function, R_{vv}, for a velocity series at a specific point in steady flow, is defined as:

$$R_{vv}(\tau) = \frac{\overline{v'(t)\, v'(t-\tau)}}{\overline{v'^2}} \tag{3}$$

Figure 5 shows the autocorrelation functions for the subsample of cylinder pairs (A and B), for a test at $Re_d = 335$. By virtue of the position relative to each cylinder, a strong periodic signal, representative of the vortex shedding process, was obtained. It is expected that cylinder interactions will affect the dominant frequencies of each cylinder diameter, in contrast to single cylinders. To illustrate this difference, a Single Cylinder Prediction (SCP) curve, based on the Strouhal number, S_t (Roshko 1954) is included for each diameter. The Strouhal number, S_t, non-dimensionalises shedding frequency using the cylinder diameter and mean reach-scale velocity, $\langle\overline{u}\rangle$

$$S_t = \frac{f_s d}{\langle\overline{u}\rangle} \tag{4}$$

The variation of R_{vv} for each pair of cylinders (see Figure 1c) clearly shows that the characteristic periods are not comparable. This suggests that the structures captured in these periodic signals do not depend on their reference cylinders alone, but reflect the effect of surrounding cylinders.

Analysing the R_{vv} curves presented in Figure 5, the location of each cylinder with reference to the map for $U^*(x, y)$ (see Figure 2a) reveals important information about the coherence of each sampled point. Cylinder A for $d = 4$ mm is relatively isolated, which explains the smaller period, when compared with B, which is located directly downstream from a larger cylinder (12 mm), and thus shows a larger period.

For the $d = 8$ mm cylinders, A is located downstream from a group of larger cylinders, and B is isolated. The frequency (i.e. reciprocal of the dominant period) of B is larger than that for A, as expected, but also larger than the Single Cylinder Prediction (SCP). The autocorrelation function for cylinder $d = 12$ mm-A, does not show a strong coherent component, but its location is close to that of cylinder $d = 15$ mm-A, which has a larger characteristic period than its SCP. This suggests that cylinders $d = 12$ mm-A and $d = 15$ mm-A are interacting and thus generating a larger coherent structure. In contrast, cylinders $d = 12$ mm-B and $d = 15$ mm-B, are both isolated, but the first has a characteristic period similar to the SCP while the second has a higher frequency than the SCP. Cylinder $d = 20$ mm-A has a larger period than $d = 20$ mm-B, though both are smaller than the SCP. The periods shown in Figure 5, highlight the inadequacy of single cylinder predictions to characterise flow structures in cylinder arrays, and emphasise the influence of cylinder interactions on the temporal features of flow structures.

Figure 6a shows the shedding frequencies, f_s, obtained as the dominant component of the Power Spectral Density function for all 32 reference cylinders, using Welch's method (Cryer et al. 1987) for all Re_d tested. A proportionality trend between the shedding frequency and Re_d, confirms a faster mass exchange between recirculation regions and far wakes, for increasing values of Re_d. It should be noted that the shedding frequency values presented in Figure 6a result from cylinder interactions and cannot be linked to a specific diameter. If the estimated shedding frequencies are non-dimensionalised using the diameter of each reference cylinder, the distribution of Strouhal numbers shown in Figure 6b is obtained. The variability of St suggests that reference cylinder diameter is not an appropriate length scale to non-dimensionalise the shedding frequency and scale of vortices from interacting cylinders. Even though the separation mechanism still obeys the same principle (instability and separation of a laminar boundary layer, Schlichting and Gersten 2017). Interacting cylinders behaving as single bluff bodies have a complex, non-linear behaviour that depends on more factors than a single reference diameter: orientation, distance and diameter ratio of the interacting cylinders. Indeed finding appropriate length scales to non-dimensionalise shedding frequencies from interacting cylinders is important to characterise cylinder arrays. This question is addressed below by exploring the connection between these periodic features, flow scales and the RandoSticks morphology.

Further, Figure 6a shows that the scatter in the estimates of f_s seems to increase with Re_d within the range $100 < Re_d < 500$. For $Re_d \approx 665$, almost all sample points have the same shedding frequency, confirming the existence of the transverse seiching. Seiching is defined as transverse surface waves in cylinder flows, when the vortex shedding frequency comes into phase with the natural standing wave frequency of the channel, determined by its geometry (Defina and Pradella 2014). The predominant in-phase frequency ($Re_d \approx 665$) is divided into multiple dominant frequencies at $Re_d = 865$.

Note that the existence of a dominant frequency due to seiching does not preclude the existence of other relevant coherent structures; just that the seiching frequency is the strongest signal captured by the velocity series. Further analyses are needed to decompose the main frequencies from these velocity series, as multiple shedding frequencies are usually found from cylinder-pair interactions (Sumner 2010). It can be seen that even for cylinders that can be considered isolated, there is little agreement between estimated shedding frequencies and single-cylinder predictions (see Figure 5). The variability in estimates of f_s, particularly for $Re_d < 500$, suggest a broader distribution of dominant frequencies, and therefore time scales, for the flow structures passing through the area of analysis. These results suggest that cylinder interactions influence the characteristic time scales of the flow structures. Single cylinder predictions of characteristic periods using the Strouhal number, based on the reach-average velocity, $\langle \overline{u} \rangle$, clearly overlook the range of flow structures generated by cylinder interactions. Consequently, any meaningful characterisation of flow structures in obstructed flows should consider the local velocity field. The local velocity is used to quantify the Strouhal number, as shown in Figure 6b. The variability in the estimation supports the idea that interacting cylinders and isolated ones are not scalable. A way of characterising the length scale of flow structures generated by interacting cylinders is necessary and presented in this paper.

RandoSticks length scales

In engineering practice, it is useful to connect the characteristic length scale of the flow structures to morphological descriptors of the vegetated array. Contrary to previous hypotheses proposing the characteristic flow scale to be the representative diameter in cylinder arrays (Nepf 1999, White and Nepf 2003), Figures 5 and 6a shows no correlation between cylinder diameters and the estimated shedding frequencies for the RandoSticks configuration. The variability in the estimates of f_s clearly suggests a range of flow scales broader than the diameter distribution.

As an alternative, Tanino and Nepf (2008b) suggested that the average edge-to-edge distance between a cylinder and its nearest-neighbour is the relevant flow scale, provided such distances are smaller than the representative diameter. Physically, flow structures are constrained by the space between cylinders, and only considering a nearest neighbour overlooks the existence of larger flow structures, resulting from cylinder interactions, as the results from Figure 6a suggest. A nearest-neighbour can be an interacting element and not a spatial constraint. Hence, if inter-stem spacing is the relevant constraint limiting the size of flow structures, a way to define spacing that considers the range of possible flow structures generated from element interactions is needed.

This study proposes the use of a Delaunay criterion (De Loera et al. 2010) to define the edge-to-edge spacing distribution between neighbouring cylinders. This criterion defines valid spaces (i.e. neighbours) as any group of 3 cylinders (cf. points) that can have a circumscribed circle without containing any other interfering cylinder. The concept of a circumscribed circle as the space that can contain a flow structure is justified by the results from Turbulent momentum fluxes (see Figure 4), which shows that these fluxes are isotropic in a double-averaged sense, i.e. turbulent scales have on average, the same dimensions in the streamwise and transverse direction.

An area of the PIV Field of View (dotted rectangle in Figure 1c), is chosen to illustrate the difference between the nearest-neighbour (NN) and Delaunay (DN) definition of inter-stem (edge-to-edge) spacing, and shown in Figure 7a and 7b, respectively. It can be seen that the NN spacing distribution is a subset of the DN distribution. The Delaunay spacing considers larger spaces that can contain flow structures generated by interacting cylinders. The probability density and cumulative distribution for both spacing definitions, for the entire RandoSticks array is shown in Figure 7c. As expected, a wider range of spacing is obtained using the Delaunay criterion.

As shown in the previous section, shedding frequency and length scale estimates for the characterisation of array morphology should consider cylinder interactions, the local velocity field, and their effects on the flow structures that are generated. To describe the range of flow structures existing in the RandoSticks configuration, the reciprocal of the shedding frequencies presented above (i.e. the characteristic time scale of the integral structures) is multiplied by the travelling velocity of the vortices, as suggested by Taylor's frozen turbulence hypothesis (Taylor 1938), to obtain the characteristic length scales, Λ_t, of the RandoSticks configuration.

Following these assumptions, the characteristic time scales, $T = 1/f_s$ (i.e. periods) of each dominant frequency shown in Figure 6a, are multiplied by a velocity scale, u_l to obtain an estimate of the characteristic length scale of the RandoSticks distribution.

$$\Lambda_t = T u_l \tag{5}$$

The next question is how to define u_l to compute length scales. For single-cylinder studies, the approach velocity is commonly used. However, Maryami et al. (2020) argues that this is not an appropriate velocity scale to non-dimensionalise shedding frequencies in single cylinders. Similarly, the use of a reach-scale mean velocity, $\langle\overline{u}\rangle$, does not represent the actual local travel velocities of the vortices whose shedding frequencies are presented in Figure 6a. It is proposed to specify u_l as the velocity at the end of the recirculation region, to scale the shedding frequency, as it better represents the local travel velocity of the vortices (Maryami et al. 2020; Roshko 1955). Following this approach, the distribution of length scales for all 32 cylinders presented in Figure 8a is obtained.

The variation of the mean Λ_t with Re_d shows that the distribution of length scales is independent of Reynolds number, at least for the range of flows tested. Physically, the consistency in the estimation of larger flow structures confirms the existence of cylinder interactions, and the formation of flow structures from multiple cylinders acting as clusters. The characteristic length scales presented in Figure 8a are larger than those expected from the RandoSticks cylinder diameter distribution.

To illustrate this, Figure 8b compares the morphological scales measured directly from the RandoSticks configuration, namely, the diameter distribution; the nearest-neighbour (NN) and Delaunay (DN) spacing distributions; and those obtained from the statistical analysis of the velocity series, using the local velocity field, and the 'global' velocity scale ($\langle\overline{u}\rangle$). The length scales obtained using local velocities have a broader range than those obtained from the distribution of cylinder diameters, and nearest-neighbour (NN) spacing; but show remarkable agreement to those from the Delaunay (DN) distribution.

This confirms that the characteristic length scales of flow structures in the RandoSticks configuration are determined by cylinder interactions, and constrained by the space available between neighbouring obstructions, not the nearest elements or stem diameters. This agrees with the results presented in Stovin et al. (2022), where numerical simulations of dispersion in different cylinder arrays, with different diameter distributions, showed that dispersion coefficients scale more consistently with cylinder spacing than cylinder diameter.

The RandoSticks configuration presented here, and those analysed in Stovin et al. (2022) are representative of a wide range of vegetation species, consequently the Delaunay criterion is expected to apply for configurations with similar density and diameter distributions. However, for cases outside of this range, i.e. sparse $\varphi \to 0$ and dense $\varphi \to 1$, the present results cannot be directly extrapolated. For sparse configurations, cylinders behave independently as distances prevent interactions. For dense arrays the space between elements is not large enough to allow the formation of coherent structures. The relevant length scales in this cases are, therefore, the diameter d, for sparse configurations; and the nearest-neighbour spacing s_n for dense arrays.

Based on the previous considerations, the RandoSticks configuration belongs to a range of intermediate vegetation densities wherein cylinders are close enough to interact and affect the formation of flow structures. Within this intermediate range, the most appropriate estimation of the range of flow structures can be obtained via a Delaunay triangulation. Therefore, for engineering practice, in vegetated arrays of similar reach-average characteristics to the RandoSticks configuration (e.g. winter Typha latifolia) the quantification of inter-stem spacing using a Delaunay criterion, should be used to estimate flow scales.

CONCLUSIONS

This paper presents the results from a comprehensive study of velocity fields, using non-intrusive optical techniques, in a random cylinder array designed to mimic the features of natural species. The maps of time-averaged streamwise and transverse velocities show the location and extent of obstructed flow features, specifically, wakes, recirculation and acceleration zones. These were found to have minimal variation with Reynolds number, such that the time-averaged flow field is constant with Re_d.

The same RandoSticks configuration was tested for an extensive range of flow regimes, characterised by the interaction of the obstructions with the flow field. The results show that the variation of turbulent momentum fluxes with Re_d is governed by vortex dynamics. A decreasing trend for turbulent momentum fluxes, $\left\langle \overline{u_i'u_i'} \right\rangle$ in the range $Re_d < 300$ suggests turbulent production caused by vortex decay and a transition to three-dimensional turbulence. For $Re_d > 300$, the behaviour of turbulent momentum fluxes supports previous hypotheses of a transition to 3D turbulence in the cylinder wakes. This increase in small-scale turbulence and the transition to turbulence in the formation region is in agreement with the decrease in streamwise dispersive fluxes as the extent of the recirculation region tends to decrease.

Based on the characterisation of average momentum fluxes, it was found that turbulent momentum fluxes can be considered isotropic in a double-average framework. Normalised longitudinal dispersive fluxes are significantly higher than transverse fluxes, and both are primarily determined by array morphology. Shear turbulent and dispersive fluxes are negligible in a double-average sense, but are a good indicator of local momentum and mass transfers, particularly the absence of momentum transfer between wakes with opposing signs in the Reynolds stress. Wake interactions can be interpreted depending on the sign of local shear virtual stresses.

An in-depth analysis of the range of characteristic flow scales, based on estimations of the main periodic component from velocity series over the flow field, reveals the existence of flow structures with a broader range of scales than those associated with the diameter distribution. The distribution of flow structures was found to resemble closely the distribution of edge-to-edge spacing between neighbouring cylinders, defined using a Delaunay criterion. The range of flows structures measured indicates that the size of coherent structures is determined by a variety of non-linear cylinder interactions, from isolated elements, to interacting cylinders forming clusters. The size of these structures is limited by the inter-stem spacing. Estimates of flow structures using a Delaunay criterion are expected to be valid for an 'intermediate' range of vegetation densities, similar to the RandoSticks configuration. For the range of flows tested, the range of flow scales is independent of Re_d. For engineering applications, such as estimating dispersion coefficients for pollutant transport, characterising flow resistance, and non-dimensionalising hydrodynamic parameters, it is proposed that practitioners employ a distribution of inter-stem spacing using a

Delaunay criterion.

Data Availability Statement

- All data, models, or code that support the findings of this study are available from the corresponding author upon reasonable request.

Acknowledgments

The authors would like to express their gratitude to the technical personnel of the Water Laboratory at the University of Sheffield, particularly Mr. Joe Milner for his invaluable help during the set-up stage of the experimental system.

Funding Information

This work was supported by a University of Sheffield Studentship for the completion of a PhD degree for the first author, and EPSRC (Grant No. EP/P012027/1). For the purposes of open access, the authors have applied a Creative Common Attribution (CC BY) license to any Author Accepted Manuscript version arising.

APPENDIX I. NOTATION

The following symbols are used in this paper:

Latin Symbols

a = Frontal Facing Area of Vegetation per Unit Volume [m^{-1}];

d = Cylinder Diameter [m];

f_s = Shedding Frequency [1/s];

g = Acceleration due to gravity [m/s^2];

h = Flow depth [m];

k = Turbulent Kinetic Energy [m^2/s^2];

n = Cylinder Density [cylinder/m^2];

p = Pressure [N/m^2];

R_{vv} = Autocorrelation function of the transverse velocity [-];

Re_d = Cylinder Reynolds Number [-];

s = Mean edge-to-edge Spacing using a Delaunay Criterion [m];

s_n = Mean edge-to-edge Spacing to nearest neighbour [m];

S_t = Strouhal number [-];

T = Characteristic Time Scale obtained from the Autocorrelation function [s];

$U(x, y)$ = Time-averaged Streamwise Velocity $\overline{u} \equiv U(x, y)$ [m/s];

U = Double-Averaged Velocity $U \equiv \langle \overline{u} \rangle$ [m/s];

u_i = Instantaneous Velocities in Tensor notation, $(u_1, u_2, u_3) \equiv (u, v, w)$ [m/s];

u_l = local velocity scale at the end of the recirculation region [m/s];

$V(x, y)$ = Time-averaged Transverse Velocity $\overline{v} \equiv V(x, y)$ [m/s];

X_{rs} = Streamwise Distance from Seeding Injection Point [m];

x_i = Coordinates in Tensor notation, $(x_1, x_2, x_3) \equiv (x, y, z)$ [m];

Y_{rs} = Lateral distance of the flume [m];

Greek Letters

β = Flume Slope [-];

ΔX = Longitudinal Dimension of the PIV Field of View [m];

ΔY = Transverse Dimension of the PIV Field of View [m];

δ_{ij} = Kronecker Delta [-];

ϵ = Porosity [-];

Λ_t = Flow Length Scale obtained from the Autocorrelation function[m];

ν = kinematic viscosity [m^2/s];

ρ = water density [kg/m^3];

φ = Solid Volume Fraction [-];

Mathematical symbols and operators

$\overline{\cdot}$ = Time Averaging [-];

$\langle \cdot \rangle$ = Volume Averaging [-];

θ^+ = Standard Deviation of the time series represented by the variable θ, $\theta^+ = \sqrt{\overline{\theta'^2}}$ [-];

θ^* = Normalised version of the dimensional quantity θ [-];

$\left\langle \overline{u_i}'' \overline{u_j}'' \right\rangle$ = Dispersive Fluxes cf. form-induced stresses [m^2/s^2];

$\left\langle \overline{u'u'} \right\rangle$ = Turbulent Fluxes cf. Reynolds stresses [m^2/s^2];

REFERENCES

Computar (2018). "Specifications H6Z0812 Camera Lens, <https://computar.com/resources/files_v2/219/H6Z0812_Spec0604.pdf>. Accessed on July 31, 2022.

Corredor-Garcia, J. L. (2023). "Solute transport in flow through random emergent vegetation." Ph.d thesis, The University of Sheffield, (February).

Corredor-Garcia, J. L., Stovin, V., and Guymer, I. (2022). "Spatio-temporal characterisation of hydrodynamics and mixing processes in obstructed flows using optical techniques." *Proceedings of the 39th IAHR World Congress*, Granada, Spain, 5140–5149.

Cryer, J. D., Bendat, J. S., and Piersol, A. G. (1987). *Random Data: Analysis and Measurement Procedures*. John Wiley and Sons, 4th edition.

Csanady, G. T. (1973). *Turbulent Diffusion in the Environment*. D. Reidel Publishing Company, Dordrecht, Holland, 1st edition.

De Loera, J. A., Rambau, J., and Santos, F. (2010). *Triangulations: Structures for Algorithms and Applications*. Springer Verlag, Berlin, 1st edition.

Defina, A. and Pradella, I. (2014). "Vortex-induced cross-flow seiching in cylinder arrays." *Advances in Water Resources*, 71, 140–148.

FLIR (2018). "Technical Reference Blackfly®s BFS-U3-23S3.

Gerrard, J. H. (1978). "The Wakes of Cylindrical Bluff Bodies at Low Reynolds Number." *Philosophical Transactions of the Royal Society of London. Series A, Mathematical and Physical Sciences*, 288(1354), 351–382.

Giménez-Curto, L. A. and Corniero Lera, M. A. (1996). "Oscillating turbulent flow over very rough surfaces." *Journal of Geophysical Research: Oceans*, 101(C9), 20745–20758.

Higham, J. and Brevis, W. (2019). "When, what and how image transformation techniques should be used to reduce error in particle image velocimetry data?." *Flow Measurement and Instrumentation*, 66, 79 – 85.

Hinze, J. O. (1975). *Turbulence*. McGraw Hill, 2nd edition.

Jalonen, J. and Järvelä, J. (2014). "Estimation of drag forces caused by natural woody vegetation of different scales." *Journal of Hydrodynamics*, 26(4), 608–623.

Jirka, G. H. and Uijttewaal, W. S. J. (2004). "Shallow Flows: a definition." *Shallow Flows*, G. H. Jirka and W. S. J. Uijttewaal, eds., CRC Press, Taylor and Francis Press, Delft, 3 – 11.

Juang, J. Y., Katul, G. G., Siqueira, M. B., Stoy, P. C., and McCarthy, H. R. (2008). "Investigating a hierarchy of eulerian closure models for scalar transfer inside forested canopies." *Boundary-Layer Meteorology*, 128(1), 1–32.

Kiya, M., Tamura, H., and Arie, M. (1980). "Vortex shedding from a circular cylinder in moderate-reynolds-number shear flow." *Journal of Fluid Mechanics*, 141(4), 721–735.

Maryami, R., Ali, S. A. S., Azarpeyvand, M., and A., A. (2020). "Turbulent flow interaction with a circular cylinder." *Physics of Fluids*, 32(1), 1 – 18.

Nepf, H. M. (1999). "Drag , turbulence , and diffusion in flow through emergent vegetation." *American Geophysical Union*, 35(2), 479–489.

Nepf, H. M. (2012). "Flow and transport in regions with aquatic vegetation." *Annual Review of Fluid Mechanics*, 44, 123–142.

Nepf, H. M., Mugnier, C. G., and Zavistoski, R. A. (1997a). "The effects of vegetation on longitudinal dispersion." *Estuarine, Coastal and Shelf Science*, 44(6), 675–684.

Nepf, H. M., Sullivan, J. A., and Zavitoski, R. A. (1997b). "A model for diffusion within an emergent plant canopy." *Limnology and Oceanography*, 42(8), 1735–1745.

Nikora, V., Ballio, F., Coleman, S., and Pokrajac, D. (2013). "Spatially Averaged Flows over Mobile Rough Beds: Definitions, Averaging Theorems, and Conservation Equations." *Journal of Hydraulic Engineering*, 139(8), 803–811.

Nikora, V., McLean, S., Coleman, S., Pokrajac, D., McEwan, I., Campbell, L., Aberle, J., Clunie, D., and Koll, K. (2007). "Double-Averaging Concept for Rough-Bed Open-Channel and Overland Flows: Applications." *Journal of Hydraulic Engineering*, 133(8), 884–895.

Nishihara, G. N. and Terada, R. (2010). "Spatial variations in nutrient supply to the red algae Eucheuma serra (J. Agardh) J. Agardh." *Phycological Research*, 58(1), 29–34.

Pope, S. B. (2000). *Turbulent Flows*. Cambridge University Press, 1st edition.

Raupach, M. R., Coppin, P. A., and Legg, B. J. (1986). "Experiments on scalar dispersion within a model plant canopy part I: The turbulence structure." *Boundary-Layer Meteorology*, 35(1-2), 21–52.

Ricardo, A. M. (2014). "Hydrodynamics of turbulent flows within arrays of circular cylinders." Ph.d thesis, Instituto Superior Técnico Lisboa & École Polytechnique Fédérale de Lausanne,

Ricardo, A. M., Canelas, R. B., and Ferreira, R. M. (2016a). "Characterization of vortex interaction with lagrangian coherent structures." *River Flow - Proceedings of the International Conference on Fluvial Hydraulics, RIVER FLOW 2016*, 135–140.

Ricardo, A. M., Franca, M. J., and Ferreira, R. M. L. (2016b). "Turbulent flows within random arrays of rigid and emergent cylinders with varying distribution." *Journal of Hydraulic Engineering*, 142(9), 1–6.

Ricardo, A. M., Koll, K., Franca, M. J., Schleiss, A. J., and Ferreira, R. M. L. (2014a). "The terms of the turbulent kinetic energy budget within random arrays of emergent cylinders." *Water Resources Research*, 50, 4131–4148.

Ricardo, A. M., Martinho, M., Sanches, P., Franca, M., and Ferreira, R. (2014b). "Experimental characterization of drag on arrays of rough cylinders." *3rd IAHR Europe Congress, Book of Proceedings*, Porto, Portugal, 1–10.

Ricardo, A. M., Sanches, P. M., and Ferreira, R. M. (2016c). "Vortex shedding and vorticity fluxes in the wake of cylinders within a random array." *Journal of Turbulence*, 17(11), 999–1014.

Righetti, M. and Armanini, A. (2002). "Flow resistance in open channel flows with sparsely distributed bushes." *Journal of Hydrology*, 269(1-2), 55–64.

Roshko, A. (1954). "On the Development of Turbulent Wakes from Vortex Streets." *National Advisory Committee for Aeronautics*, 1191, 1–25.

Roshko, A. (1955). "On the wake and drag of bluff bodies." *J. Aeronaut. Sci.*, 22, 124 – 132.

Schlichting, H. and Gersten, K. (2017). *Boundary-Layer Theory*. Springer-Verlag, Berlin, 9th edition.

Schott (2017). "DURAN® Datasheet. Tubing, rods and capillaries made of borosilicate glass 3.3.

Shilton, A. (2000). “Potential application of computational fluid dynamics to pond design.” *Water Science and Technology*, 42(10-11), 327–334.

Shucksmith, J., Boxall, J., and Guymer, I. (2007). “Importance of advective zone in longitudinal mixing experiments.” *Acta Geophysica*, 55(1), 95–103.

Simon, A., Bennett, S. J., and Neary, V. S. (2004). “Riparian Vegetation and Fluvial Geomorphology: Problems and Opportunities.” *Riparian Vegetation and Fluvial Geomorphology Vol. 8*, S. J. Bennett and A. Simon, eds., AGU, 1–10.

Sonnenwald, F., Hart, J. R., West, P., Stovin, V. R., and Guymer, I. (2017). “Transverse and longitudinal mixing in real emergent vegetation at low velocities.” *Water Resources Research*, 53(1), 961–978.

Stovin, V. R., Sonnenwald, F., Golzar, M., and Guymer, I. (2022). “The impact of cylinder diameter distribution on longitudinal and transverse dispersion within random cylinder arrays.” *Water Resources Research*, 58(4), e2021WR030396 e2021WR030396 2021WR030396.

Sumner, D. (2010). “Two circular cylinders in cross-flow: A review.” *Journal of Fluids and Structures*, 26(6), 849–899.

Tanino, Y. and Nepf, H. M. (2008a). “Laboratory Investigation of Mean Drag in a Random Array of Rigid, Emergent Cylinders.” *Journal of Hydraulic Engineering*, 134(1), 34–41.

Tanino, Y. and Nepf, H. M. (2008b). “Lateral dispersion in random cylinder arrays at high Reynolds number.” *Journal of Fluid Mechanics*, 600, 339–371.

Tanino, Y. and Nepf, H. M. (2009). “Laboratory investigation of lateral dispersion within dense arrays of randomly distributed cylinders at transitional Reynolds number.” *Physics of Fluids*, 21(4), 1–10.

Taylor, G. I. (1922). “Diffusion by continuous movements.” *Proceedings of the London Mathematical Society*, s2-20(1), 196–212.

Taylor, G. I. (1938). “The Spectrum of Turbulence.” *Proceedings of the Royal Society A: Mathematical, Physical and Engineering Sciences*, 164(919), 476–490.

Thielicke, W. and Sonntag, R. (2021). “Particle Image Velocimetry for MATLAB: Accuracy and enhanced algorithms in PIVlab." *Journal of Open Research Software*, 9, 1–14.

Thielicke, W. and Stamhuis, E. J. (2014). "PIVlab – Towards User-friendly, Affordable and Accurate Digital Particle Image Velocimetry in MATLAB." *Journal of Open Research Software*, 2, 1–10.

White, B. L. and Nepf, H. M. (2003). "Scalar transport in random cylinder arrays at moderate Reynolds number." *Journal of Fluid Mechanics*, 487, 43–79.

Williamson, C. H. K. (1991). "Three-Dimensional Aspects and Transition of the Wake of a Circular Cylinder." *Turbulent Shear Flows 7*, 7, 173–194.

List of Figures

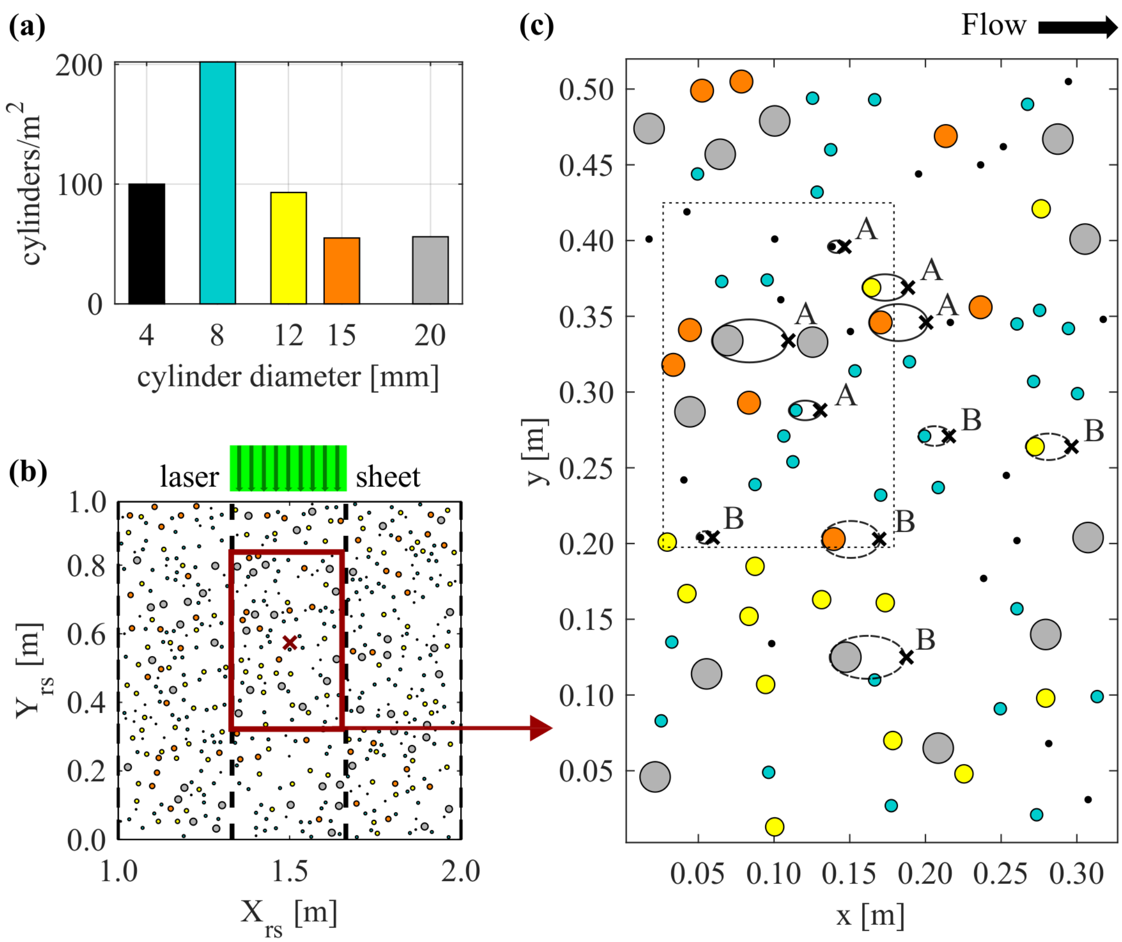

Fig. 1. **a)** RandoSticks Diameter distribution **b)** RandoSticks plate and location of the PIV FoV using global coordinates (X_{rs}, Y_{rs}). **c)** Detailed view of the PIV FoV with reference cylinders (marked by ellipses) for flow scales analysis using local coordinates (x, y), and reference area (dotted rectangle) for inter-stem spacing illustration. The × symbols represent the points marking the limit of the recirculation area, based on the location reported in single cylinders studies.

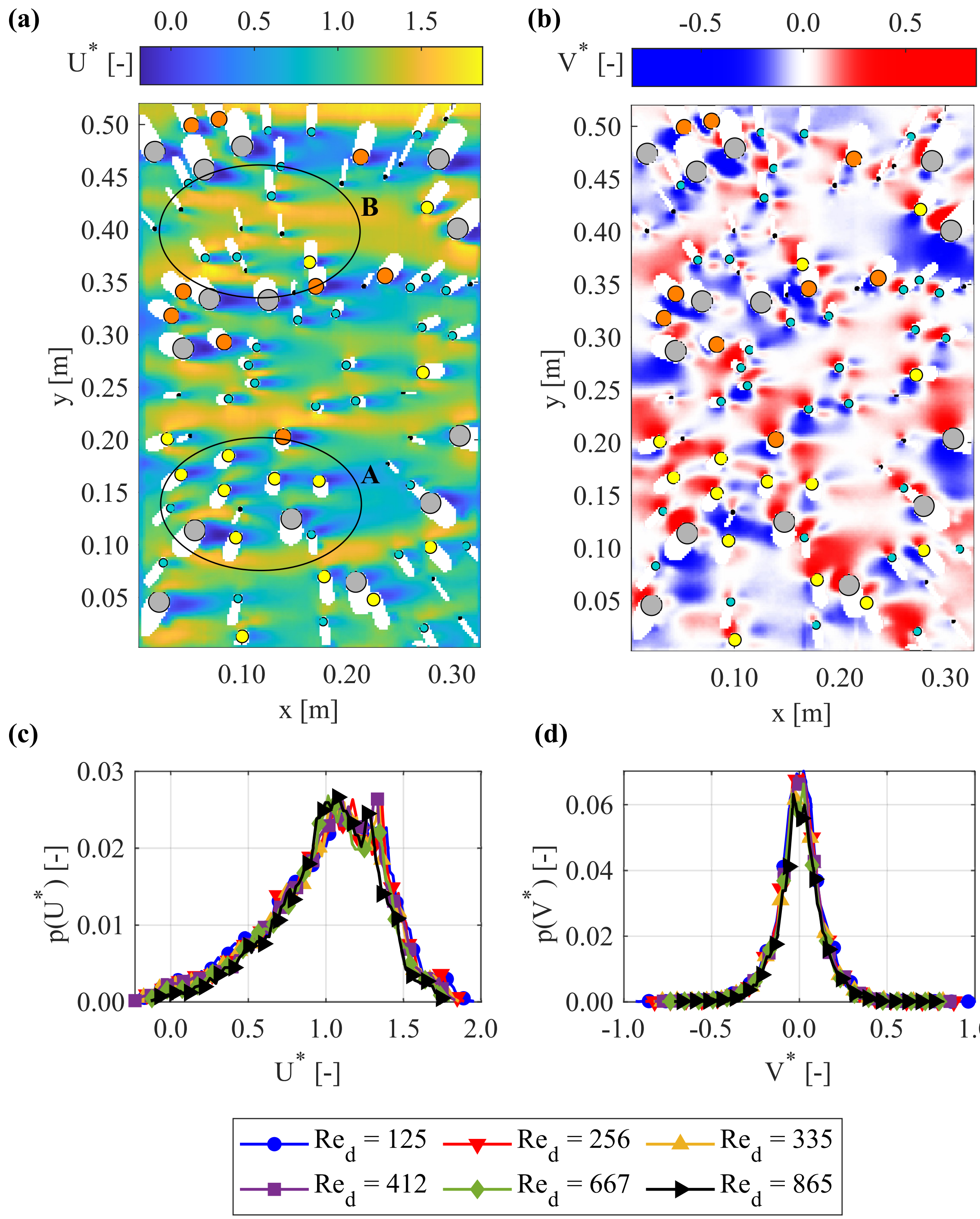

Fig. 2. Non-dimensional **a)** time-averaged streamwise velocity, $U^*(x, y)$ and **b)** time-averaged transverse velocity, $V^*(x, y)$ for Re_d = 335. Probability distribution of the time-averaged maps of non-dimensionalised **c)** streamwise and **d)** transverse velocities, for all Re_d

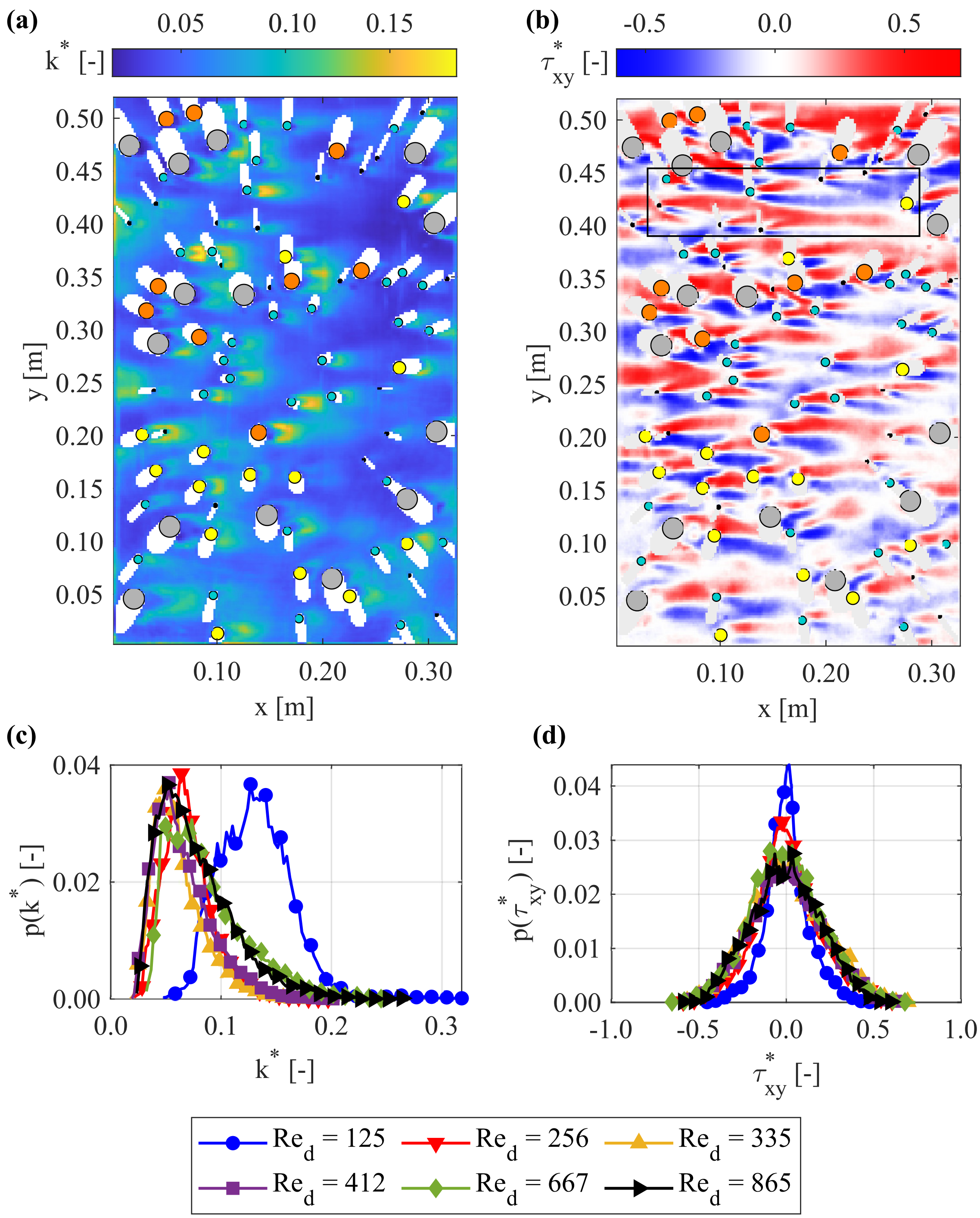

Fig. 3. Non-dimensional **a)** Turbulent Kinetic Energy, $k^*(x, y)$ and **b)** shear Reynolds stresses, $\tau^*_{xy}(x, y)$ for $Re_d = 335$. Probability distribution of the time-averaged maps of non-dimensionalised **c)** Turbulent Kinetic Energy and **d)** Shear Reynolds stresses, for all Re_d

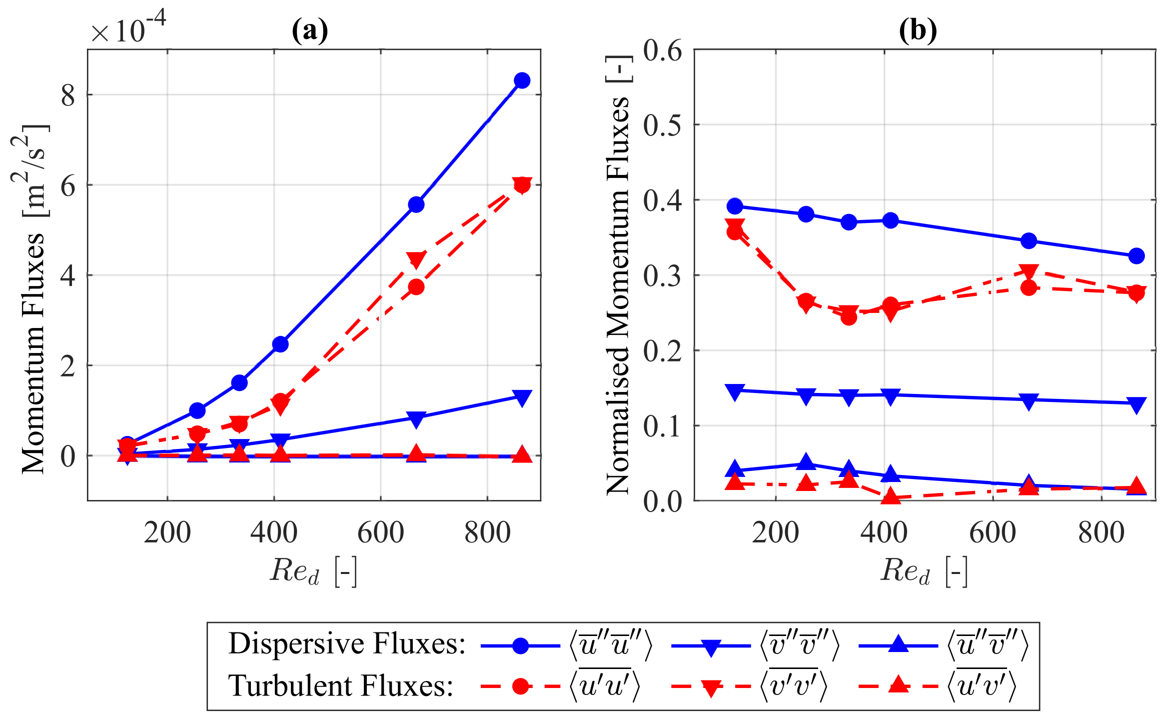

Fig. 4. Variation of **a)** dimensional dispersive (-) and turbulent (- -) fluxes; and **b)** dispersive (-) and turbulent (- -) fluxes fluxes, normalised by mean velocity, with Re_d

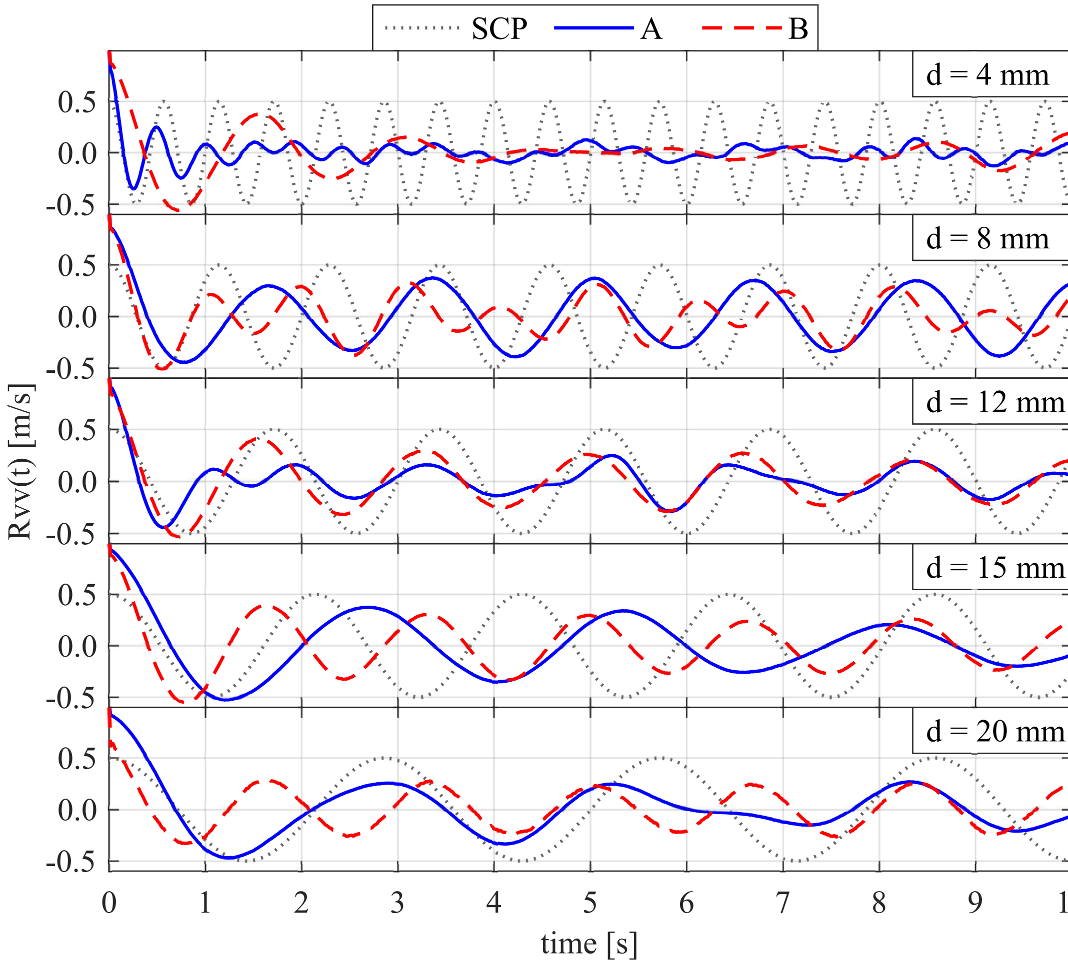

Fig. 5. Transverse velocity autocorrelation functions for a sample of cylinders, at Re_d = 335, and comparison with their respective Single Cylinder Predictions (SCP).

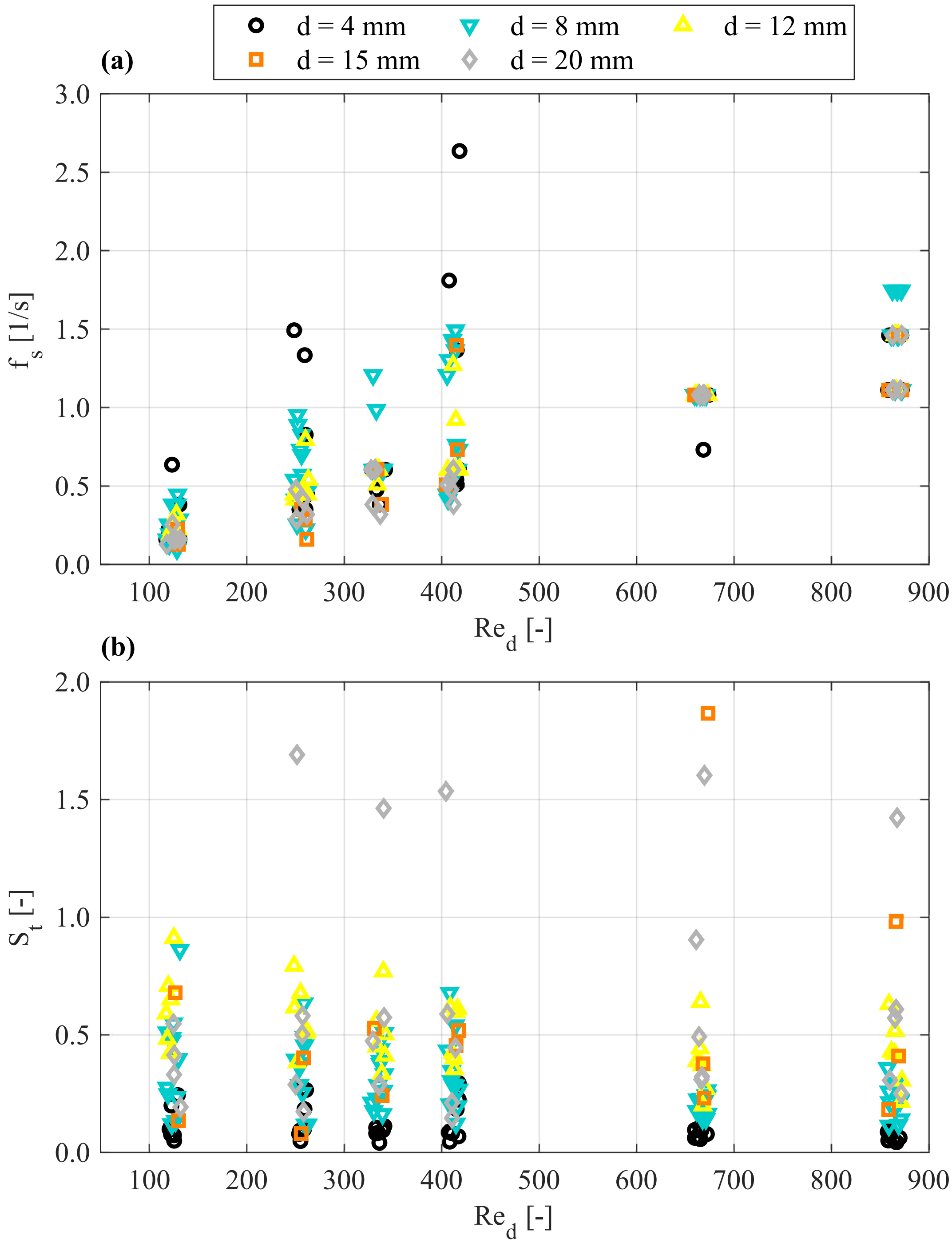

Fig. 6. a) Variation of shedding frequency, f_s, from the velocity spectra. **b)** Variation of Strouhal numbers, from shedding frequencies, using the reference cylinder diameter and local velocities as length and velocity scales, respectively.

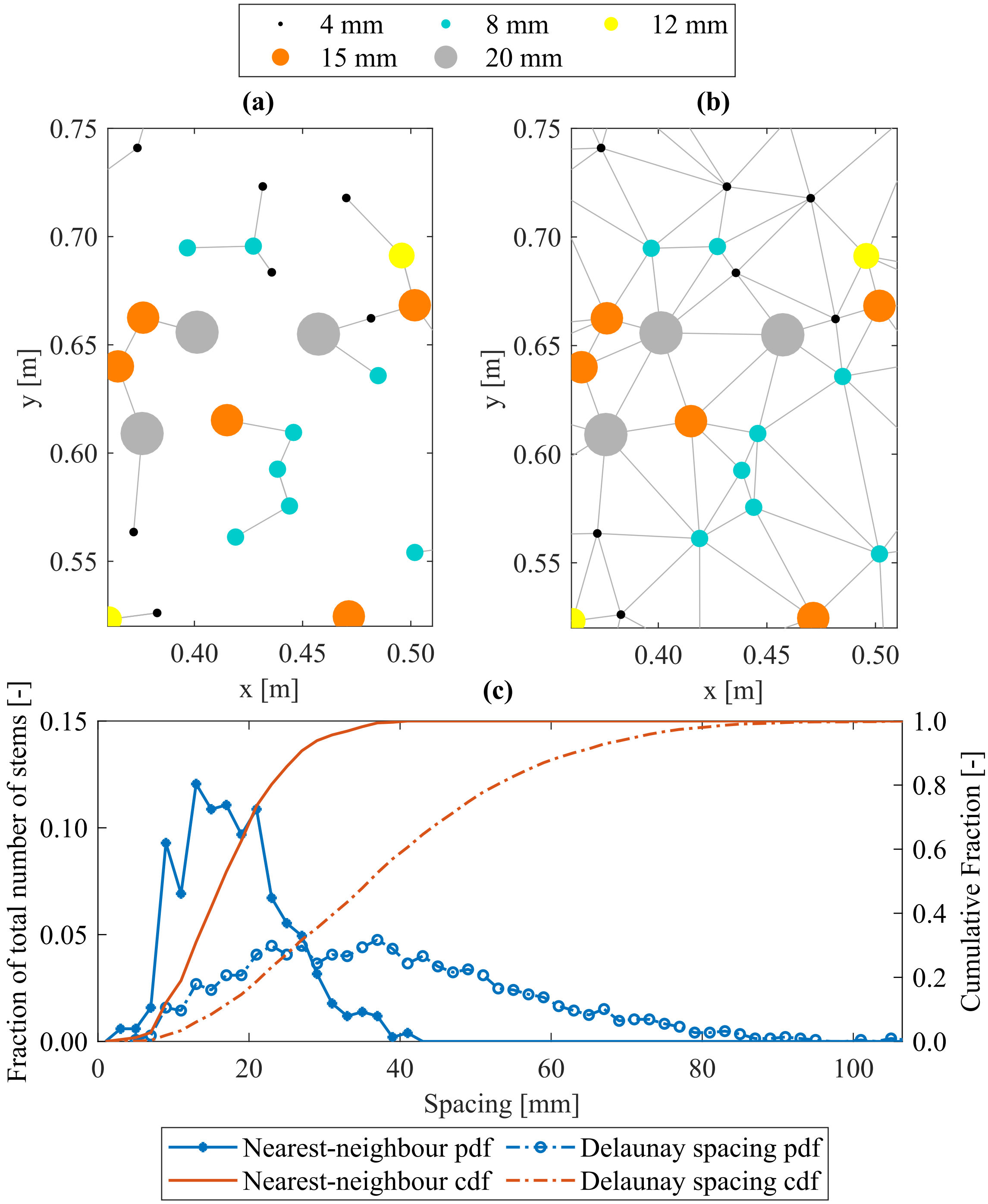

Fig. 7. **a)** Nearest-neighbour (NN) and **b)** Delaunay (DN) inter-stem spacing distributions. **c)** Probability and cumulative functions for NN and DN spacing distributions.

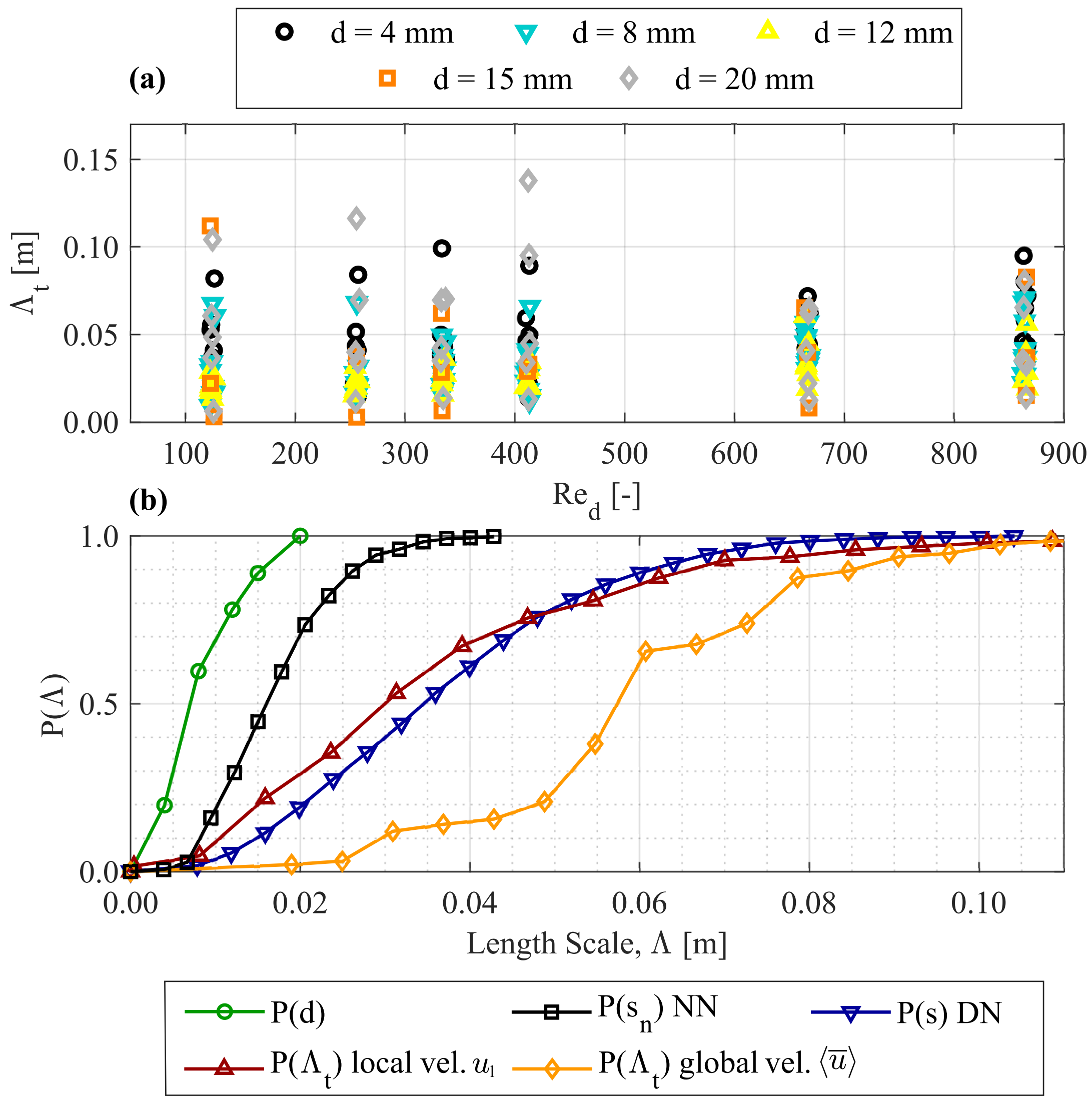

Fig. 8. a) Variation of point-based estimates of length scales, Λ_t, with respect to stem Reynolds number, Re_d, and **b)** density and cumulative Distribution functions for Λ_t, for local and global estimates of velocity.